A statistical model of false negative and false positive detection of phase singularities

Vincent Jacquemet

[1] *Institut de Génie Biomédical, Départment de Pharmacologie et Physiologie, Université de Montréal, Montréal, Canada.*

[2] *Centre de recherche, Hôpital du Sacré-Coeur, Montréal, Canada.*

The complexity of cardiac fibrillation dynamics can be assessed by analyzing the distribution of phase singularities (PS) observed using mapping systems. Interelectrode distance, however, limits the accuracy of PS detection. To investigate in a theoretical framework the PS false negative and false positive rates in relation to the characteristics of the mapping system and fibrillation dynamics, we propose a statistical model of phase maps with controllable number and locations of PS. In this model, phase maps are generated from randomly distributed PS with physiologically-plausible directions of rotation. Noise and distortion of the phase are added. PS are detected using topological charge contour integrals on regular grids of varying resolutions. Over 100 millions realizations of the random field process are used to estimate average false negative and false positive rates using a Monte-Carlo approach. The false detection rates are shown to depend on the average distance between neighboring PS expressed in units of interelectrode distance, following approximately a power law with exponents in the range 1.14 to 2 for false negatives and around 2.8 for false positives. In the presence of noise or distortion of phase, false detection rates at high resolution tend to a non-zero noise-dependent lower bound. This model provides an easy-to-implement tool for benchmarking PS detection algorithms over a broad range configurations with multiple PS.

The spatio-temporal dynamics of cardiac fibrillation is characterized by anatomical and functional reentries that contribute to perpetuate the arrhythmia. Phase mapping is a technique to assess the complexity of the dynamics and identify the location of reentries. This approach is applicable to computer simulations, optical mapping experiments as well as electrical recordings. Phase singularities are points where all values of phase converge. They correspond to the core of spiral waves and they represent potential targets for therapeutic catheter ablation. Localization of phase singularities from a limited set of electrodes is challenging. The lack of spatial resolution may result in false positive or false negative detections. This paper investigates the theoretical basis of false detection of phase singularities in a square mapping grid. A statistical model of randomly generated phase maps with controllable number of phase singularities is proposed. In this model, false positive and false negative rates are shown to be a function of the average distance between neighboring phase singularities expressed in units of interelectrode distance.

I. INTRODUCTION

Atrial fibrillation is a common arrhythmia observed as multiple electrical wavelets propagating over the atrial surface. These wavelets may be self-sustained or generated by one or a few stable rotors or by the automatic activity of ectopic foci.[1,2] Phase mapping[3–5] is often used as dimension reduction technique for monitoring atrial activity from a wide-field of view in computer simulations and clinical electrical mapping. The fibrillation dynamics is analyzed by tracking phase singularities (PS).[6–8] Clinical relevance of PS localization has recently been established in clinical trials targeting rotors for catheter ablation of atrial fibrillation.[9,10]

PS analysis is performed in three steps. First, phase maps are computed from recorded or simulated signals.[11] In simulations, the time course of the membrane potential can be used to define the phase through time-delayed embedding[12,13] or Hilbert transform.[14] These methods can be extended to estimate the phase in unipolar and bipolar electrograms.[15–17] The second step concentrates on one phase map at a time and identifies PS. The algorithm depends on the geometrical structure of the mapping system. Methods have been developed

for square grids,[8] triangular meshes[18] and mapping catheters.[16] This paper will focus on this problem. The last step consists in tracking PS trajectories to determine their stability and life span.[19] Very short-lived PS may be tagged as false positive and discarded.

Application to human atrial mapping necessarily involves a trade-off between the number of signals recorded by the mapping catheter and PS detection accuracy. The spatial resolution (inter-electrode distance) required for detecting a rotor using a multi-electrode catheter has been investigated in computer simulations, synthetic and clinical signals.[20,21] Spatial wavelength, measured as the distance between consecutive wave fronts, appeared to be the major constraint for accurate rotor detection,[21] confirming previous theoretical predictions.[22] The focus of these studies was the clinical problem of identifying a single rotor or focal activation.

In this paper, a statistical model of phase maps with multiple randomly-located PS is proposed. The model incorporates the effect of noise and distortion of the phase. Phase maps are regularly discretized using a large range of resolutions. Then, PS detection is performed and the number of false positives and false negatives is exactly determined. Monte-Carlo simulations are run to determine the false detection rates as a function of PS density and electrode density. The simplicity of this theoretical approach enables averaging over the large number of realizations needed to derive the scaling laws that give the mapping resolution required to keep false detection rates below a tolerance.

II.   METHODS

A.   Phase singularities in continuous phase maps

A phase map $\theta(\mathbf{x})$ is a continuous, smooth, angle-valued function defined on the plane, except at a finite number of points $\{\mathbf{x}_k\}$, $k = 1, \ldots n$, called phase singularities (PS).[6,11] The value of $\theta(\mathbf{x})$ is in $[-\pi, \pi)$. The topological charge of the PS at $\mathbf{x}_k$ is defined as[12]

$$q_k = \frac{1}{2\pi} \oint_\Gamma \nabla\theta \cdot \mathrm{d}\boldsymbol{\ell} \, , \tag{1}$$

where the contour integral follows a closed non-intersecting counter-clockwise oriented curve Γ surrounding $\mathbf{x}_k$ but no other PS.

This integral is calculated by parametrizing the curve Γ with the function $\mathbf{r}(t)$, $t \in [0, 1]$,

such that $\mathbf{r}(0) = \mathbf{r}(1)$, which gives

$$q_k = \frac{1}{2\pi} \int_0^1 \frac{\mathrm{d}}{\mathrm{d}t} \theta(\mathbf{r}(t)) \, \mathrm{d}t \ . \tag{2}$$

The angle-valued function $\theta(\mathbf{r}(t))$ is not continuous as a real function and will be "un-wrapped" to form a continuous real function equivalent to $\theta(\mathbf{r}(t))$ modulo 2π.

We will use the following notations: $\mathrm{mod}_{2\pi}(x) \in [0, 2\pi)$ is the value of x modulo 2π. The wrapping function $\mathcal{W}(x) = \mathrm{mod}_{2\pi}(x + \pi) - \pi$ transforms a real value into an angle in the range $[-\pi, \pi)$. Note that $\mathcal{W}(-x) = -\mathcal{W}(x)$. The unwrapping operator $\mathcal{U}[f]$ adds appropriate 2π jumps to an angle-valued function $f(t)$ to make it continuous as a real function. In particular, $\mathcal{W}(\mathcal{U}[f](t)) = f(t)$.

As a result, after unwrapping of the phase θ, the integral (2) becomes

$$q_k = \frac{1}{2\pi} \int_0^1 \frac{\mathrm{d}}{\mathrm{d}t} \mathcal{U}[\theta(\mathbf{r}(t))] \, \mathrm{d}t = \frac{1}{2\pi} \left(\mathcal{U}[\theta \circ \mathbf{r}](1) - \mathcal{U}[\theta \circ \mathbf{r}](0) \right) , \tag{3}$$

where the circle $\circ$ denotes the composition of functions. This shows that q_k is an integer and that calculating topological charges comes down to unwrapping the phase along closed paths.

The case $q_k = 0$ means that the PS is removable by appropriate definition of $\theta(\mathbf{x}_k)$. Cases with $|q_k| > 1$ have been observed in cell cultures and simulations,[23] but they remain extremely rare. We will assume that $q_k = \pm 1$ for all PS.

The contour integral (1) can be used to detect PS. If the curve Γ encloses a region that contains n_+ PS with charge $+1$ and n_- PS with charge -1, the integral is $q = n_+ - n_-$. Based only on the knowledge of q, we can predict that inside Γ there are $|q| = |n_+ - n_-|$ PS, each of them with a charge of $\mathrm{sign}(q) = \mathrm{sign}(n_+ - n_-)$. Even when the integral is calculated analytically, matching PS with opposite charges cancel each other. The number of false negative detections is therefore $2 \min(n_+, n_-)$. On the other hand, false positive detection never occurs when the continuous phase map is known.

B. Phase singularities in discretized phase maps

In experimental and simulation studies, the phase is known only at a finite number of points. Here, the mapped area considered will be a L-by-L square. For numerical computations, we will take $L = 1$ and reintroduce L at the end through dimensional analysis. The

mapping system consists of a $(K+1)$-by-$(K+1)$ grid of electrodes with regular interelectrode spacing of $\Delta x = L/K$, as illustrated in Fig. 1A. The value of K will be varied from 1 to 100. The resulting spatially sampled phase map is a matrix $\theta_{i,j} = \theta(i\Delta x, j\Delta x)$ for $i, j \in \{0, \ldots K\}$.

PS detection from a discretized phase map is based on an estimate of the integral (1) through phase unwrapping. The shortest closed path is composed of the grid points $(i, j) \rightarrow (i+1, j) \rightarrow (i+1, j+1) \rightarrow (i, j+1) \rightarrow (i, j)$ forming a square element, as shown in Fig. 1A. The sequence of phases $(\phi_0, \phi_1, \phi_2, \phi_3, \phi_4) = (\theta_{i,j}, \theta_{i+1,j}, \theta_{i+1,j+1}, \theta_{i,j+1}, \theta_{i,j})$ is the discrete equivalent of the function $\theta \circ \mathbf{r}$.

To transform a sequence of phases $(\phi_0, \phi_1, \ldots)$ into an unwrapped sequence $(\mathcal{U}\phi_0, \mathcal{U}\phi_1, \ldots)$, we first set $\mathcal{U}\phi_0 = \phi_0$ and then each step $\mathcal{U}\phi_k - \mathcal{U}\phi_{k-1}$ is taken to be the smallest step (in absolute value) among $\phi_k - \phi_{k-1}$, $\phi_k - \phi_{k-1} + 2\pi$ and $\phi_k - \phi_{k-1} - 2\pi$, thus minimizing the gradient. This smallest step is equal to $\mathcal{W}(\phi_k - \phi_{k-1})$. The cumulative sum of these steps is then computed. This procedure is implemented in Matlab in the function `unwrap` and is widely used in signal processing.

The topological charge $q_{i,j}$ within the square element located at (i, j) can be written by applying (3) to the unwrapped sequence of phases $(\phi_0, \ldots, \phi_4)$:

$$2\pi\, q_{i,j} = \mathcal{U}\phi_4 - \mathcal{U}\phi_0 = \mathcal{W}(\theta_{i+1,j} - \theta_{i,j}) + \mathcal{W}(\theta_{i+1,j+1} - \theta_{i+1,j})$$
$$+ \mathcal{W}(\theta_{i,j+1} - \theta_{i+1,j+1}) + \mathcal{W}(\theta_{i,j} - \theta_{i,j+1}) . \quad (4)$$

A uniform shift of all phases by $-\theta_{i,j}$ does not affect the gradient of the phase. This motivates the following definitions:

$$\alpha_{i,j} = \mathcal{W}(\theta_{i+1,j} - \theta_{i,j}) \tag{5}$$

$$\beta_{i,j} = \text{mod}_{2\pi}(\theta_{i+1,j+1} - \theta_{i,j}) \tag{6}$$

$$\gamma_{i,j} = \mathcal{W}(\theta_{i,j+1} - \theta_{i,j}) \tag{7}$$

These 3 variables are phase differences that fully characterize the local phase gradient. The special status of the variable β will soon be apparent. With these definitions we have

$$2\pi\, q_{i,j} = \alpha_{i,j} + \mathcal{W}(\beta_{i,j} - \alpha_{i,j}) - \gamma_{i,j} - \mathcal{W}(\beta_{i,j} - \gamma_{i,j}) . \tag{8}$$

5

The equality (8) is verified because

$$\mathcal{W}(\beta_{i,j} - \alpha_{i,j}) = \mathcal{W}\Big(\mathrm{mod}_{2\pi}(\theta_{i+1,j+1} - \theta_{i,j}) - \mathcal{W}(\theta_{i+1,j} - \theta_{i,j})\Big) \tag{9}$$

$$= \mathcal{W}(\theta_{i+1,j+1} - \theta_{i+1,j} + k \cdot 2\pi) \;=\; \mathcal{W}(\theta_{i+1,j+1} - \theta_{i+1,j}) \tag{10}$$

where k is an integer. The term $\mathcal{W}(\beta_{i,j} - \gamma_{i,j})$ is handled similarly, with the help of the relation $\mathcal{W}(-x) = -\mathcal{W}(x)$.

Let us define $g(x) = x + \mathcal{W}(\beta - x)$. Since $x \in [-\pi, \pi)$ and $\beta \in [0, 2\pi)$, the graphical representation of $\mathcal{W}(\beta - x)$ shows that $g(x) = \beta$ if $\beta - x < \pi$ and $g(x) = \beta - 2\pi$ if $\beta - x \geq \pi$. An alternative formulation is $g(x) = \beta - 2\pi H(\beta - x - \pi)$ where $H(x)$ is the right-continuous Heaviside step function. Consequently, (8) becomes

$$q_{i,j} = H(\beta_{i,j} - \gamma_{i,j} - \pi) - H(\beta_{i,j} - \alpha_{i,j} - \pi) \ . \tag{11}$$

Note that $|q_{i,j}| \leq 1$ since $H(x) \in \{0, 1\}$.

Computer implementation is straightforward: from a $(K + 1) \times (K + 1)$ matrix θ, the $K \times K$ matrices α, β and γ are computed using (5)–(7); then a non-zero $q_{i,j}$ can be identified with the exclusive-or conditional statement: $\beta_{i,j} - \alpha_{i,j} < \pi$ XOR $\beta_{i,j} - \gamma_{i,j} < \pi$; the signs of the detected PS are finally given by (11). The condition for PS detection is therefore represented by a region delimited by two planes in the (α, γ, β) space.

PS detection can also be performed on larger paths. If M is a small integer ($M = 1, 2, 3$ here) that divides K, the grid may be subdivided into K/M-by-K/M non-overlapping groups of M-by-M square elements (Fig. 1B–C). Each true PS can be in only one of these K^2/M^2 square elements, which will facilitate the definition of false negatives and avoid boundary effects. The integral along the borders of any M-by-M square is equal to the sum of the integrals over each of these M^2 square elements

$$q_{i,j}^{(M)} = \sum_{k=0}^{M-1} \sum_{k'=0}^{M-1} q_{iM+k, jM+k'} \tag{12}$$

where $i, j \in \{0, \ldots K/M - 1\}$. Obviously, $q_{i,j}^{(1)} = q_{i,j}$. The decomposition as a sum is not only exact in the continuous, analytical case, but also in the discretized case as it can be seen from (4). Note that $|q_{i,j}^{(M)}| \leq M^2$, and if $M > 1$, $|q_{i,j}^{(M)}|$ may be > 1. Practically, it was always ≤ 3.
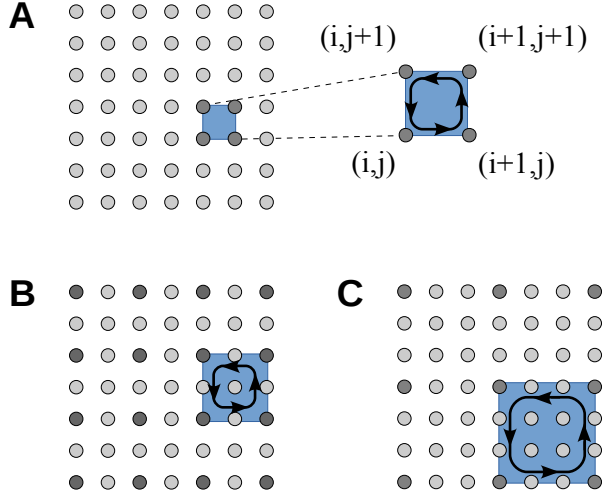
FIG. 1. Mapping grid with $K = 6$ with interelectrode distance Δx. (A) Square element ($M = 1$) and its associated path of length $4\,\Delta x$ to evaluate the contour integral that gives the topological charge. (B) One of the $K^2/M^2 = 9$ non-intersecting paths of length $8\,\Delta x$ when $M = 2$. (C) Same for $M = 3$ with a path of length $12\,\Delta x$.

C.   Random generation of phase maps

The objective is to create a large number of continuous phase maps with multiple PS with random locations and charges. These phase maps will then be sampled at different spatial resolutions to serve as a benchmark for the evaluation of PS detection methods.

A configuration of PS is determined by the list of PS locations and charges (z_k, q_k) for $k = 1, \ldots n$, where the position is defined for convenience by a complex number z_k with real and imaginary parts in $[0, L]$, and where $q_k = \pm 1$. The number of PS, n, will be varied between 1 and 16, thus covering the range from few macro-reentrant rotors to multiple transient wavelet breakups. Scaling laws and asymptotic expansions will enable extrapolation to even more PS.

PS locations will be independently and uniformly distributed over the L-by-L square. Note that this is not intended to represent PS distribution over time, which is often observed to be concentrated in specific regions due to structural or functional heterogeneity.[24,25] Instead, the uniform distribution is assumed to model the statistics of all PS configurations measured in all experiments performed using the mapping system, including situations where

pairs of PS are very close just after creation or before annihilation. In other words, it represents an ensemble statistics and not a temporal statistics. The outcome will be an assessment of the mapping system and of the PS detection algorithm.

The selection of the charges uses minimization of electrostatic energy to prevent nearest neighbor PS from having the same charge. For fixed positions $\{z_k\}$, the energy is defined as in Herlin et al.[26]

$$E(\{q_k\}) = \sum_{k=1}^{n} \sum_{k'=k+1}^{n} \frac{q_k q_{k'}}{|z_k - z_{k'}|} \ . \tag{13}$$

The charge q_1 is randomly set to $+1$ or -1. Then the energy is minimized over the 2^{n-1} remaining configurations. This quadratic binary optimization problem is known to be computationally complex,[27] but for $n \leq 16$ it is easily solved by exhaustive search. The resulting charge distribution typically has nearest-neighbor PS with opposite charges and a total charge $\sum_k q_k = 0$ or ± 1. Exceptional $(< 0.01\%)$ cases with $|\sum_k q_k| > 1$ were discarded. A total of $N_{\mathrm{config}} = 10,000$ configurations were randomly created for each of the $N_{\mathrm{PS}} = 16$ values of n.

For a given configuration $\{(z_k, q_k)\}$, the phase map

$$\theta(z) = \arg \prod_{k=1}^{n} (z - z_k)^{q_k} \tag{14}$$

has been shown to have n PS located at z_k with a charge of q_k, $k = 1, \ldots n$.[28] From this analytical form, discretized maps can be generated for each of the $N_{\mathrm{grid}} = 100$ values of K. These $N_{\mathrm{config}} \times N_{\mathrm{PS}} = 160,000$ phase maps will be referred to as control phase maps.

To quantify the effect of noise or uncertainty on the determination of the phase from electrical or optical recordings, random noise is added to the phase field. We assume that the noise is distributed as a wrapped normal random variable[29] and that noise terms in different electrodes are statistically independent. The independence hypothesis corresponds to the worst case scenario since spatially correlated noise at a length scale larger that interelectrode distance would result in a local uniform shift of the phase with little impact on PS detection. The wrapped normal distribution has two convenient properties: (1) it can be easily and efficiently generated as a normal random number modulo 2π; (2) additivity: the sum of two wrapped normal distributions is a wrapped normal distribution, which is not the case for the von Mises distribution.[29] The perturbed phase map is obtained as

$$\theta_{\mathrm{noisy}}(z) = \mathcal{W}(\theta(z) + \sigma Z(z)) \ , \tag{15}$$

where $Z(z)$ are independent standard normal random variables and σ^2 determines noise variance, which means that $\theta_{\text{noisy}}(z)$ is a wrapped normal variable with mean $\theta(z)$ and standard deviation parameter σ. When $\sigma \ll 1$, θ_{noisy} is approximately distributed normally. When $\sigma \to +\infty$, and practically already when $\sigma \approx 3$, θ_{noisy} become uniform on $[-\pi, \pi)$.

For the implementation, the phase is computed using (14)–(15) in all the grids together, avoiding duplicate computations at nodes present in multiple grids. This saves about 18% of computing requirements and, more importantly, it ensures that the same sample of random noise is used at each location, e.g. at the corner nodes present in all grids. For $N_\sigma = 13$ values of σ ranging from 0.03 to 2, $N_{\text{realiz}} = 50$ realizations of the noise field are used, giving a total of $N_{\text{PS}} \times N_{\text{config}} \times N_\sigma \times N_{\text{realiz}} = 102$ million phase maps sampled at $N_{\text{grid}} = 100$ different resolutions.

In these randomly generated phase maps, the norm of the phase gradient is essentially uncorrelated to the value of phase. This may not be the case in simulations or experimental studies where variations of phase may be slower during the excitable gap or faster during depolarization, depending on the method used for calculating the phase. In order to assess the effect of increased spatial variations in phase gradient, a phase distortion function is applied point-by-point to the phase map. This distortion function $h(\theta)$ must be bijective in the domain $[-\pi, \pi)$ and is chosen to be

$$h(\theta) = \theta + c \, \sin(\theta) \tag{16}$$

where $0 \leq c < 1$ to ensure that $h'(\theta) > 0$. With increasing values of c, the phase gradient becomes steeper near the isophase line $\theta = 0$ and flatter near $\theta = \pm\pi$. For $N_c = 10$ values of c ranging from 0.05 to 0.9, the distortion functions are applied to all generated phase maps without noise, leading to another $N_{\text{PS}} \times N_{\text{config}} \times N_c = 1.6$ million maps.

Figure 2 shows examples of generated phase maps with different numbers of PS. Automatic determination of PS charges appears to assign opposite charges to nearest-neighbor PS. The absence of a characteristic length scale creates a form of self-similarity that will be exploited later to derive scaling laws. The effect of noise is obvious on the second column of panels in Fig. 2. The third column of panels illustrates how the distortion function creates regions of steeper phase gradients.
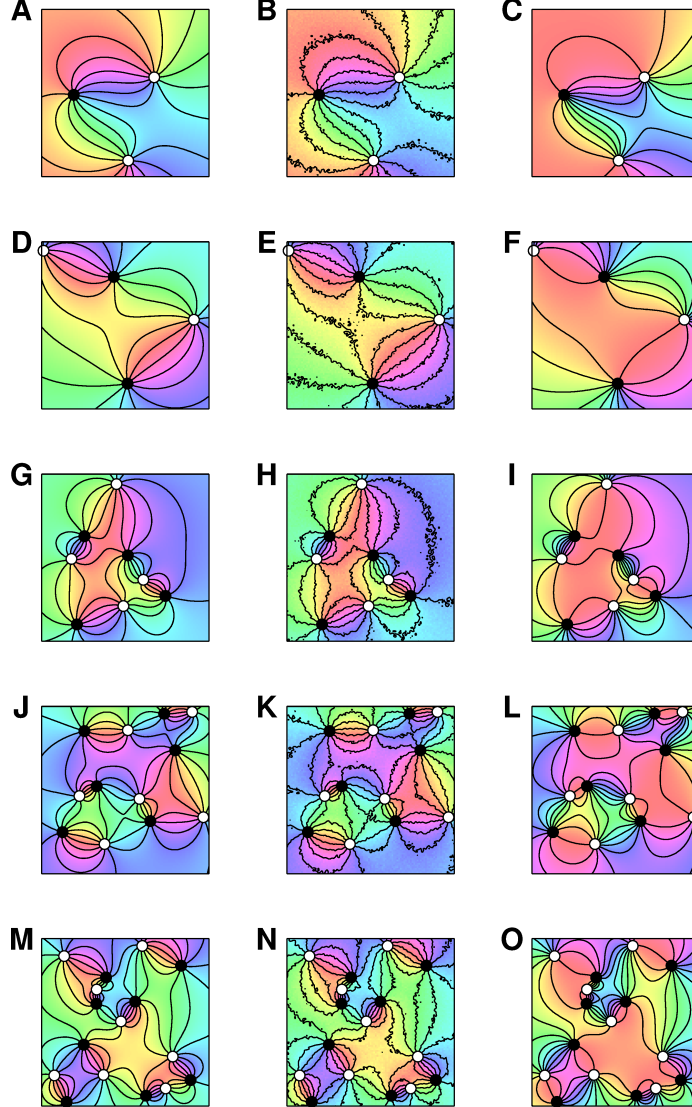
FIG. 2. Examples of randomly generated phase maps with 3, 4, 8, 12 and 16 phase singularities (PS) computed on a 101-by-101 grid. The phase is color-coded and 12 isophase lines regularly distributed over $[-\pi, \pi)$ are displayed. PS are represented as black or white circles depending on their sign (clockwise or counter-clockwise). First column: Control phase maps. Second column: Noisy phase maps with $\sigma = 0.05$. Third column: Distorted phase maps with $c = 0.8$.

D.   False positive and false negative rates

Randomly generated phase maps will be used to test PS detection methods. Since exact locations and charges of PS are known, false positive and false negative detection can be defined exactly. Consider a closed curve Γ with n_+ PS with charge $+1$ and n_- PS with

charge -1 in its interior. If an approximation of the contour integral (1) over the path Γ gives an integer q, we predict that the region enclosed in Γ has $|q|$ PS, each one with charge $\text{sign}(q)$. This is the choice that minimizes the number of PS detected.

Each detected PS is either a true positive (TP) or a false positive (FP)

$$\text{TP} + \text{FP} = |q| \ . \tag{17}$$

Each actual PS is classified as either a true positive (TP) or a false negative (FN) depending on whether it is detected or not

$$\text{TP} + \text{FN} = n_+ + n_- \ . \tag{18}$$

Thus, we have

$$\text{FN} = \text{FP} + n_+ + n_- - |q| \ . \tag{19}$$

If no PS is detected, there is no false positive, i.e. $q = 0$ implies $\text{FP} = 0$. If not, each detected PS in excess of $n_{\text{sign}(q)}$ is a false positive

$$\text{FP} = \max\left(|q| - n_{\text{sign}(q)}, 0\right) \tag{20}$$

where $n_{\text{sign}(q)} = n_+$ if $q > 0$ and n_- if $q < 0$. Combined with (19), this gives the number of false positives and false negatives as a function of detection outcome (q) and ground truth (n_+ and n_-). Note that if the integral is exactly evaluated, $q = n_+ - n_-$ and then $\text{FP} = 0$ and $\text{FN} = 2\min(n_+, n_-)$ as in the analytical case (section II A).

When PS detection is performed on a set of K^2/M^2 square paths indexed by $i, j \in \{0, \dots K/M - 1\}$ like at the end of section II B, each path is associated with a number of false positives $\text{FP}_{i,j}$ and false negatives $\text{FN}_{i,j}$. The false positive rate (FPR) is defined as the average number of false positives per square path tested

$$\text{FPR} = \frac{M^2}{K^2} \sum_{i=0}^{K/M-1} \sum_{j=0}^{K/M-1} \text{FP}_{i,j} \ . \tag{21}$$

The false negative rate (FNR) is defined as the fraction of the n PS that have not been detected

$$\text{FNR} = \frac{1}{n} \sum_{i=0}^{K/M-1} \sum_{j=0}^{K/M-1} \text{FN}_{i,j} \ , \tag{22}$$

so that $0 \leq \text{FNR} \leq 1$.

11

For each value of PS number (n), noise amplitude (σ) and grid resolution (Δx), statistics of FPR and FNR (mean and standard deviation) are calculated over $N_{\text{config}} \times N_{\text{realiz}} = 500,000$ phase maps. In control cases and after application of the distortion function, the statistics is over $N_{\text{config}} = 10,000$ phase maps.

E. Scaling law for false negatives

To better understand how the false negative rate depends on the number of PS (n) and the spatial resolution of the mapping system ($\Delta x = L/K$), a simplified situation was considered: n PS are randomly, uniformly and independently distributed in K^2 squares, and the charges are assigned such that the sum of the charges in each square is -1, 0 or $+1$. Assuming that the integral (1) is calculated exactly, this means that if m PS are in a square, the number of true positives is 0 if m is even and 1 if m is odd.

The number of PS in a given square is a binomial random variable. Calculations based on the binomial distribution show that the probability that a square is empty is

$$P_{\text{empty}} = \left(1 - \frac{1}{K^2}\right)^n , \tag{23}$$

which will be used later, and the probability that the number of PS in a square is odd is

$$P_{\text{odd}} = \frac{1}{2} - \frac{1}{2}\left(1 - \frac{2}{K^2}\right)^n . \tag{24}$$

The number of true positives (TP) is the expected number of squares that include an odd number of PS

$$\text{TP} = K^2 \, P_{\text{odd}} , \tag{25}$$

and the number of false negatives is $\text{FN} = n - \text{TP}$, so the false negative rate (FNR) is

$$\text{FNR} = 1 - \frac{K^2}{2n}\left(1 - \left(1 - \frac{2}{K^2}\right)^n\right) = \frac{n-1}{K^2} + \mathcal{O}(K^{-4}) \tag{26}$$

where the approximation is valid when interelectrode spacing is small.

To interpret that formula, consider n points uniformly randomly distributed in a L-by-L square. The natural distance in a square grid is derived from the max norm

$$\|(x, y)\|_\infty = \max(|x|, |y|) \tag{27}$$

since the distance between two points becomes the size of the smallest square that contains both points, which is a situation that leads to false negatives. Empirically, the average max-norm distance between nearest-neighbor PS is approximately equal to

$$\lambda_n = \frac{L}{2\sqrt{n-1}} \tag{28}$$

where for $2 < n \leq 16$ the error is $< 3\%$ when the average is taken over our 10,000 configurations for each value of n. The asymptotic square root behavior can be demonstrated in a more general context.[30] As a result,

$$\text{FNR} = \frac{1}{4}\left(\frac{\Delta x}{\lambda_n}\right)^2 + \mathcal{O}(\Delta x^4) . \tag{29}$$

This theoretical argument suggests that the relevant parameter for false negative occurrence is the nearest-neighbor distance between PS expressed in units of interelectrode spacing and that a power-law behavior should be expected. The advantage is that it reduces the number of independent variables from two (n and K) to one ($\Delta x/\lambda_n$).

F. Scaling law for false positives

In order to get a false positive, q must be incorrectly estimated (see section II D), which may occur when $\nabla\theta$ is so steep that the difference in unwrapped phase is larger than π in a segment of length Δx. For a horizontally-aligned short segment ($\Delta x \ll L$), this means that

$$\left|\frac{\partial\theta}{\partial x}\right| > \frac{\pi}{\Delta x} . \tag{30}$$

When the phase map is given by (14), the gradient is stronger near phase singularities. For a point z in the vicinity of z_k, the phase field is

$$\theta(z) = (-1)^{q_k} \arg(z - z_k) + \arg \prod_{k' \neq k} (z - z_{k'})^{q_{k'}} \tag{31}$$

where the equality holds modulo 2π. The second term is nearly constant around $z = z_k$ so its contribution to the gradient is neglected. Writing the real and imaginary parts as $z - z_k = x + iy$, we have $\arg(z - z_k) = \text{atan2}(y, x)$, where atan2 is the four-quadrant inverse tangent. The gradient can be explicitly expressed as

$$\left|\frac{\partial\theta}{\partial x}\right| \approx \frac{|x|}{x^2 + y^2} . \tag{32}$$

The region defined by (30) is therefore composed of two disjoint disks of radius $\Delta x/2\pi$ for each of the n PS. Its total area is $n\Delta x^2/2\pi$ if Δx is sufficiently small so that the disks corresponding to different PS do not intersect.

The fraction of Δx-long horizontal segments in high gradient regions is of the order of $(n\Delta x^2)/(2\pi L^2)$, so we may argue that the false positive rate should behave like

$$\text{FPR} \propto \left(\frac{\Delta x}{\lambda_{n+1}}\right)^2 . \tag{33}$$

We however expect the asymptotic decrease in FPR for small Δx to be steeper than that for two reasons: (1) along the four sides of a square element, two 2π jumps in opposite directions may cancel each other; and (2) by being so close to the PS, the square element may actually include the PS, which would make it a true positive. Despite these limitations, it appears plausible that in this model the false positives are mostly found in the vicinity of actual PS and that $\Delta x/\lambda_{n+1}$ is a relevant parameter to determine FPR.

III. RESULTS

A. Separating planes for PS detection

In each square element, the variables α, β and γ are computed using (5)–(7). Recall that α and γ represent the phase difference along the sides of the square, while β represents the phase difference along the diagonal of the square. The condition (11) for PS detection is based on the position in the (α, γ, β) space relative to the planes $\beta - \gamma = \pi$ and $\beta - \alpha = \pi$. Figure 3 shows the distribution of (α, γ, β) built as a 3D histogram from all the control phase maps at a given resolution ($K = 16$, 24 and 64). The two separating planes create four regions, two of which (the right and the left ones on Fig. 3) trigger PS detection. The distributions corresponding to true positives or false negatives (first row of Fig. 3) and true negatives or false positives (second row) are displayed separately. Owing to the symmetry $(\alpha, \gamma, \beta) \mapsto (-\alpha, -\gamma, 2\pi - \beta)$ associated with the change in the direction of spiral rotation, only the bottom half of the space is shown. The distributions have to be understood as modulo 2π, which means for example that in Figs. 3A–C, the small piece (false negatives) in the front near $(-\pi, 0, 2)$ is actually connected to the larger piece (true positives) in the back near $(\pi, 0, 2)$.
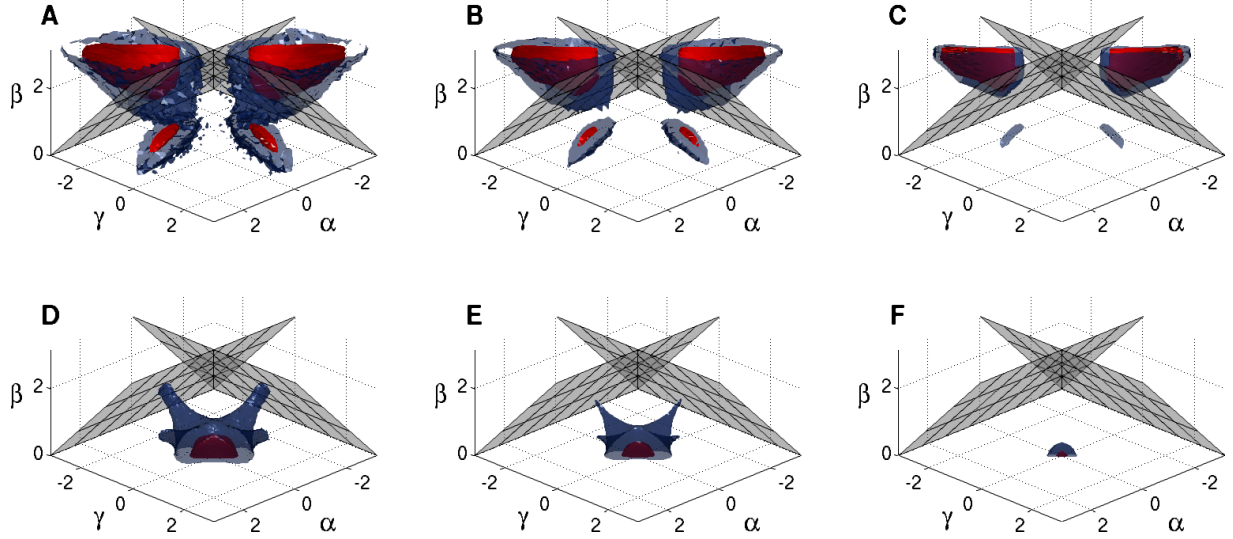
FIG. 3. Distribution of (α, γ, β) over all control phase maps with increasing spatial resolution $K = 16$ (A,D), $K = 24$ (B,E) and $K = 64$ (C,F). Panels A, B and C represent true positives and false negatives (i.e. square elements with a single PS in it) while panels D, E and F show the distribution of true negatives and false positives (where there is no PS in the square elements). The red surface contains 75% of the data points and the blue surface 95%. The separating planes $\beta - \gamma = \pi$ and $\beta - \alpha = \pi$ used for PS detection are displayed in gray.

The distribution of true positives and false negatives (panels A, B, C) is approximately centered around $(\pi/2, -2, \pi)$ and $(-2, \pi/2, \pi)$ in the region where formula (11) predicts the presence of a PS. When a higher-resolution grid of electrodes is used (panel C), the spread of the distribution is reduced and the number of false negatives decreases. The spread of the distribution however does not tend to zero at high resolution because the phase maps are scale-invariant in the vicinity of a PS.

The distribution of true negatives and false positives (panels D, E, F) is centered around $(0, 0, 0)$ and has arms pointing toward the cores of the distribution of true positives and corresponding to square elements located close to a PS. These locations are therefore more prone to false positives. As resolution increases, a larger proportion of square elements are further from PS so that the distribution becomes concentrated around the origin (panel F) and its spread tends to zero.

B. Scaling laws for false negatives and false positives

Figure 4A shows the mean false negative rate (FNR) as a function of interelectrode distance ($M = 1$) and number of PS. Each point is the average over $N_{\text{config}} = 10,000$ control phase maps. For $n = 1$ PS, there is no false negative. FNR increases with the number of PS and when mapping resolution is coarser. Motivated by the theoretical results of subsections II E and II F, non-dimensional length scales are introduced:

$$\xi = \frac{\Delta x}{\lambda_n} = \frac{2\sqrt{n-1}}{K} \qquad \text{and} \qquad \xi_c = \sqrt{\frac{n}{n-1}}\,\xi\ . \tag{34}$$

When n is large, $\xi \approx \xi_c$. These length scales conceptually represent how small interelectrode distance is as compared to the distances between PS. In a cardiac simulation context where the phase is computed at every computational node, we may have $K = 200$ and $n = 10$, leading to $\xi = 0.03$, which is the lower end of our range. On the other hand, a 4-by-4 array mapping catheter might sense the activity of $n = 1$ to 2 PS, giving a ξ value of the order of 1, the high end of our range. When FNR is expressed as a function of ξ instead of Δx, the curves for different values of the number of PS are superimposed (Fig. 4B).

The mean false positive rate (FPR) is displayed in Fig. 4C. Like FNR, FPR increases with the number of PS, but is a biphasic function of Δx. The decrease at low resolution is due to the fact that no false positive can be found in a square element that actually contains a PS. When K is small, there are fewer square elements empty of PS. This can be taken into account by defining a corrected false positive rate (FPRc)

$$\text{FPRc} = \frac{\text{FPR}}{P_{\text{empty}}} = \text{FPR} \cdot \left(1 - \frac{1}{K^2}\right)^{-n} \approx \text{FPR} \cdot \left(1 + \frac{1}{4}\xi_c^2\right)\ . \tag{35}$$

where P_{empty}, the probability of a square element to be empty, comes from (23). When ξ_c is small or if K is large, FPRc $\approx$ FPR. The resulting curves are shown in Fig. 4D. In both Figs. 4B and D, a few points associated with very small values of n and K are off the main trend. In the next subsections, only points with $n > 2$ and $K > 2$ will be displayed for the sake of clarity. The logarithmic scale will be used for false detection rates to highlight asymptotic behavior.

Since the probability of false detection can become very small, the relative standard error on the mean (RSEM) is estimated to verify whether the number of configurations generated is appropriate. The RSEM is defined as the standard deviation of the $N_{\text{config}} = 10,000$
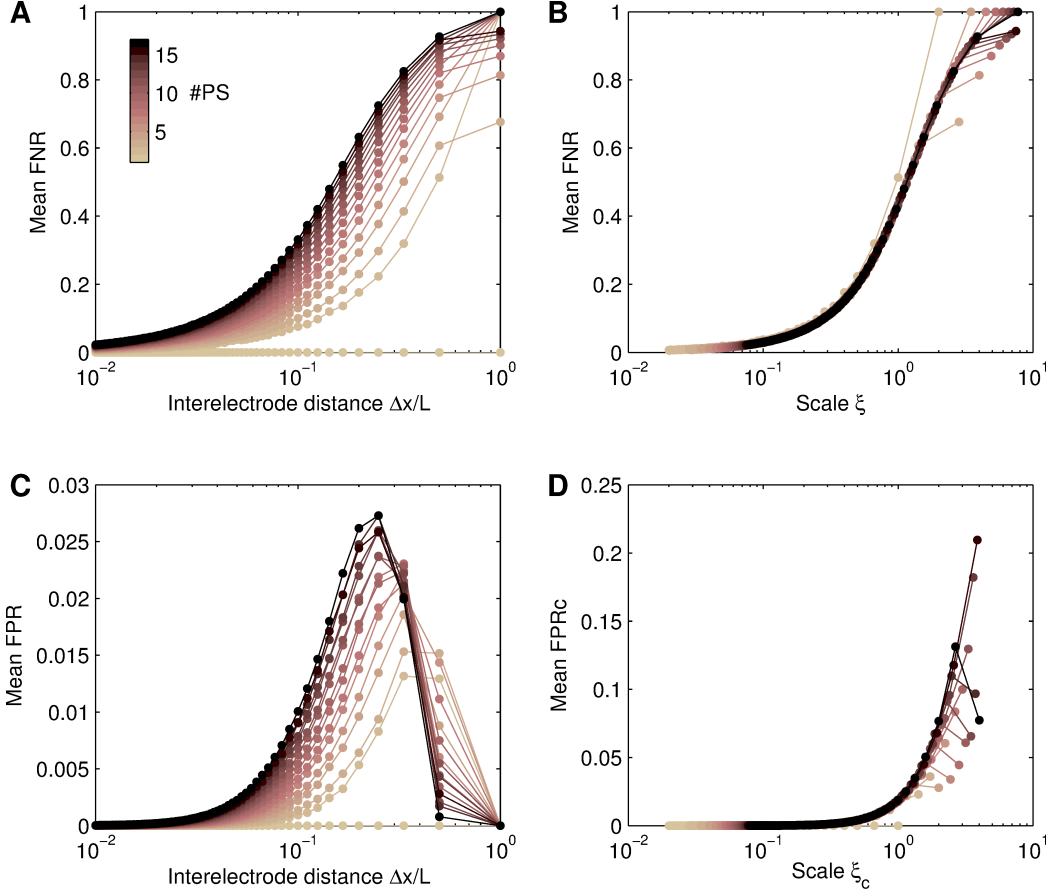
16

FIG. 4. Mean false positive and false negative rates over the control phase maps. (A) Mean false negative rate (FNR) as a function of interelectrode distance and number of PS (color-coded). (B) Same data as in panel A but expressed as a function of the scale ξ. (C) Mean false positive rate (FPR) as a function of interelectrode distance and number of PS (color-coded). (D) Mean corrected false positive rate (FPRc) as a function of the scale ξ_c.

values, divided by $\sqrt{N_{config}}$ and by the mean value. The RSEM of both FNR and FPRc appears to be proportional to $n^{-1/2}$, as shown in Fig. 5. The RSEM is higher at small length scale ξ but remains below $0.12\,n^{-1/2}$, which translates into a few percents in most cases.

C. Length of integration path and power laws

The statistical model of phase maps enables the evaluation of the advantages and disadvantages of detecting PS in M-by-M square elements (Fig. 1). This discretization of the integration path can be seen from two different perspectives.
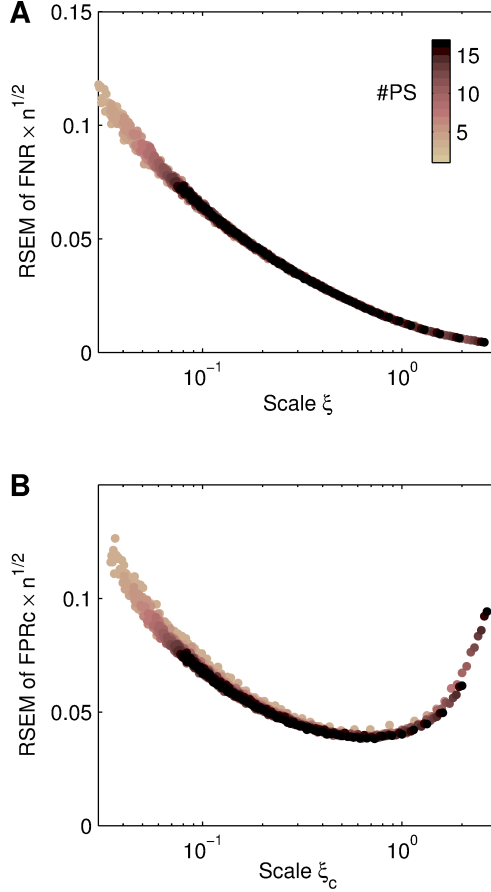
FIG. 5. Relative standard error on the mean (RSEM) of false positive rate (FNR; panel A) and corrected false negative rate (FPRc; panel B), scaled by $\sqrt{n}$ and expressed as a function of the length scale ξ or ξ_c. Each data point represents the RSEM estimated from 10,000 control phase maps at different resolutions and number of PS (color coded).

The first viewpoint is to consider a square path whose side of length Δx is subdivided into M segments to improve the accuracy of estimating the contour integral. Figure 6A shows the mean FNR as a function of $M\xi$ so the curves for $M = 1, 2, 3$ as compared at the same value of $M\Delta x$ representing the side of the square. When $M \to \infty$, the integral is calculated exactly and is equal to the expectation of $2\min(n_+, n_-)/n$ in the notations of subsection II D. This curve, displayed in black in Fig. 6A ($M = \infty$), almost coincides with the theoretical formula (29): $\text{FNR} = \xi^2/4$.

For increasing values of M, PS detection is more accurate and FNR decreases. The FNR curves follow approximately power laws with exponents 1.14, 1.43 and 1.63 for $M = 1, 2, 3$
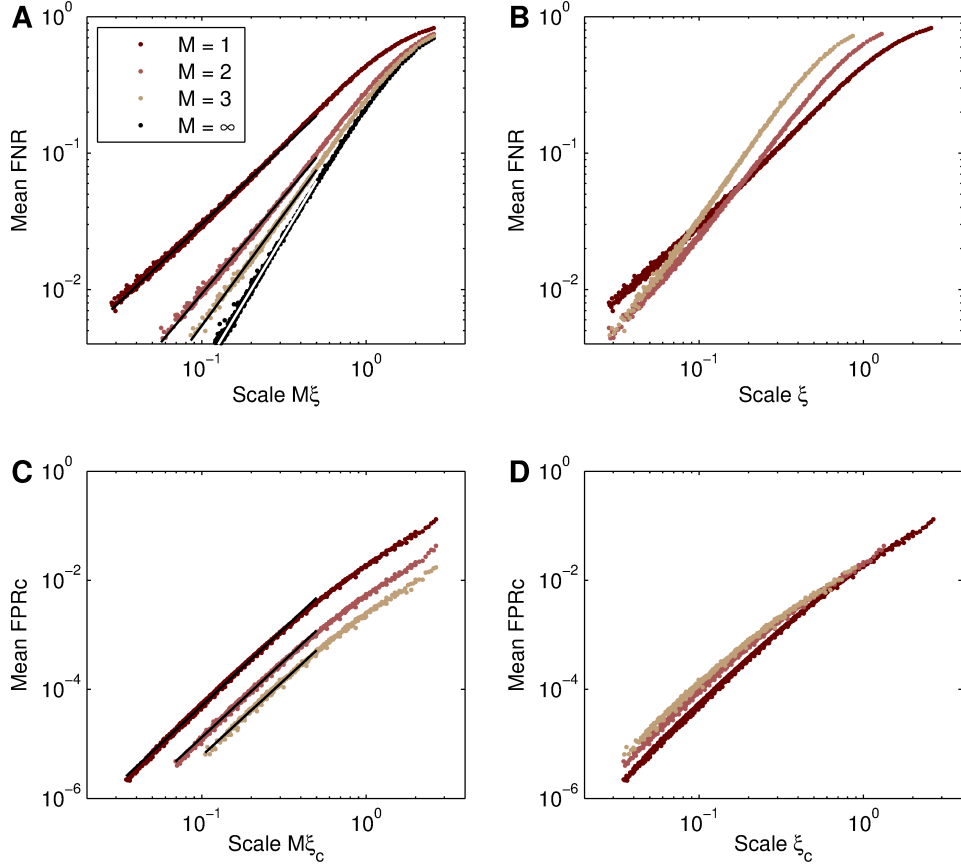
FIG. 6. False negative rates (FNR) and corrected false positive rates (FPRc) in control phase maps for different integration path lengths ($M = 1$ to 3). The case $M = \infty$ in (A) corresponds to exact integration. In (A) and (C), the scales ξ or ξ_x multiplied by M are associated with the side of the square element over which the phase gradient is integrated, while in (B) and (D) the scales ξ and ξ_c are associated with interelectrode distance (this is why the case $M = \infty$ is not present in panel B). Power law fits are drawn as black lines. The white line in (A) follows theoretical formula (29): $\text{FNR} = \xi^2/4$.

respectively. The standard errors on the exponents are < 0.01. The results for FPRc are similar, except that the exponents of the fitted power laws are steeper and of the same order of magnitude: 2.82, 2.79 and 2.77 for $M = 1, 2, 3$, with a standard error < 0.015. As anticipated, the exponent is larger than the theoretical value (33). When $M \to \infty$, FPRc is always zero so the curve is not shown.

The second viewpoint concentrates on finding the best method given a fixed number of electrodes. The false detection rates are displayed as a function of ξ (Fig. 6B,D). A square

element with $M = 3$ has an area 9 times bigger than a square element with $M = 1$. When ξ is large, the significant probability of having multiple PS in the square element makes the method with $M = 3$ less effective. When ξ is small, the exponent of the power law takes over. As a result, FNR is minimal for $M = 1$ when $\xi > 0.17$, for $M = 2$ when $0.03 < \xi < 0.17$, and for $M = 3$ when $\xi < 0.03$. According to subsection II F, false positives are more likely to occur near a PS. With large square elements, a larger proportion of these false positives (even if it is the same absolute number) are located in the vicinity of a PS. In agreement with this hand-waving argument, FPRc tends to be larger when $M > 1$.

The spatial extent of that vicinity is estimated in subsection III F. In the range $\xi_c < 0.5$, FPRc is on average 1.8 times larger when $M = 2$ and 2.4 times larger when $M = 3$ as compared to $M = 1$. This result is mitigated by the pre-factor M^2/K^2 in (21). Even if the FPRc is larger, the absolute number of false positives is still smaller by a factor $M^2/1.8 = 2.2$ for $M = 2$ and $M^2/2.4 = 3.8$ for $M = 3$.

D.   Effect of noise

In the control phase maps, the value of the phase is known exactly from an analytical formula. Real-life scenarios include noise and uncertainty that will certainly affect false detection rates. Figure 7 shows the increase in false detection rates observed after addition of noise of different variances. In the presence of noise, false detection rates do not behave as power law but instead saturate at short length scale ξ. The best method among $M = 1, 2, 3$ remains $M = 1$ at high ξ, $M = 2$ at mid-range ξ and $M = 3$ at low ξ. As compared to the control cases, the intervals of ξ for which $M = 2$ is the best method are shifted to the right by noise. For example, at $\sigma = 0.1$, $M = 2$ is the best for $0.08 < \xi < 0.23$, and at $\sigma = 0.5$, $M = 2$ is the best for $0.2 < \xi < 0.5$. Consequently, the benefits of longer integration path lengths (increasing M) in terms of FNR increase with noise variance. Noise also increases FPRc, moderately up to $\sigma = 0.5$, and then by a large amount. This corresponds to false positive detection not only near PS but also anywhere else, randomly caused by local fluctuation of phase (see subsection III F). As with control phase maps, larger integration paths ($M > 1$) slightly increase FPRc.
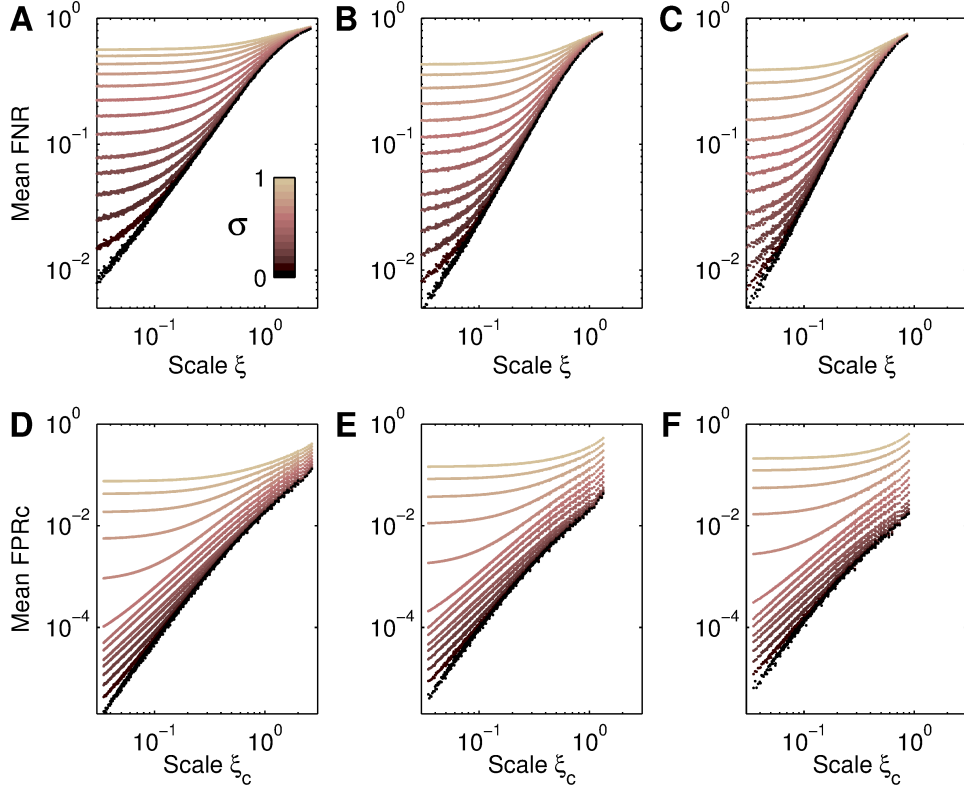
FIG. 7. Effect of noise on false negative rate (FNR) and corrected false positive rate (FPRc) as a function of length scale for values of σ ranging from 0 to 1 radian (color coded): $\sigma = 0$, 0.03, 0.06, 0.1, 0.15, and 0.2 to 1 by step of 0.1. (A)–(D) $M = 1$; (B)–(E) $M = 2$; (C)–(F) $M = 3$.

E. Effect of phase distortion

The ideal phase map for PS detection has a smooth phase gradient that is as uniform as possible. The application of the distortion function (16) creates regions of steeper gradients and regions of almost constant phase. The consequence is an increase in false detections (Fig. 8). Even a small distortion ($c = 0.05$) has a significant impact on FNR at high resolution (small ξ on panels A–C). Larger integration paths ($M > 1$) are more robust against that distortion. FPRc, on the other hand, seems less affected than FNR (panels D–F). The effect on FPRc appears also to be smaller than that of noise. Note, however, that an increase of FPRc by a factor of almost 100 is possible at low ξ.
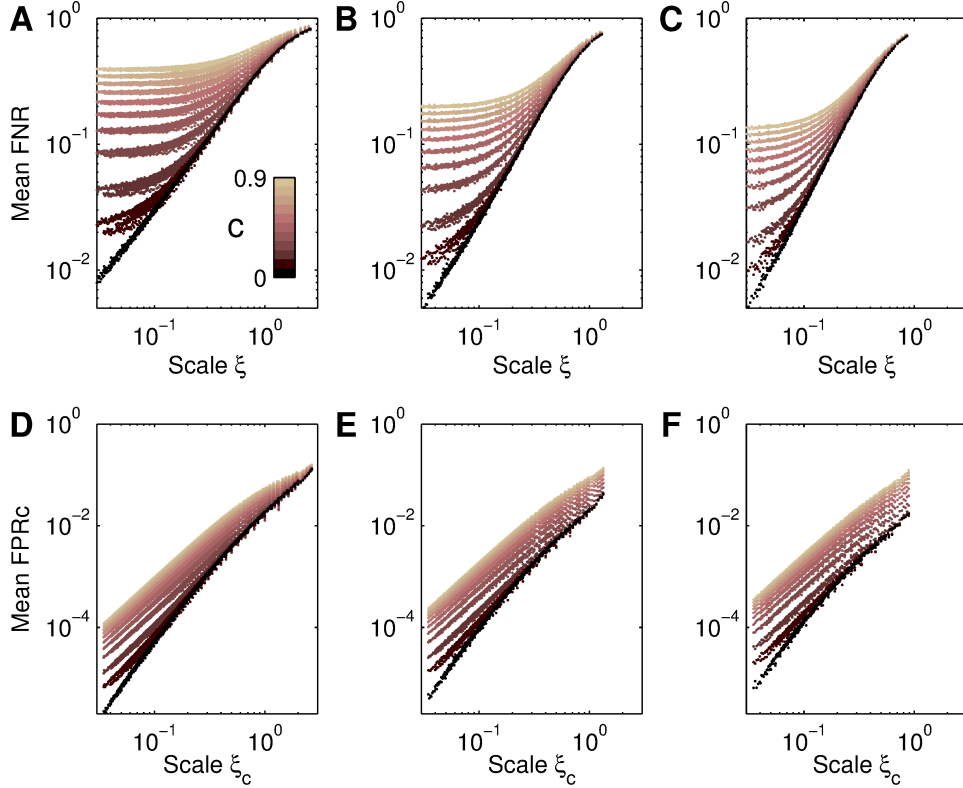
FIG. 8. Effect of phase distortion on false negative rate (FNR) and corrected false positive rate (FPRc) as a function of length scale for values of c ranging from 0 to 0.9 (color coded): $c = 0$, 0.05, and 0.1 to 0.9 by step of 0.1. (A)–(D) $M = 1$; (B)–(E) $M = 2$; (C)–(F) $M = 3$.

F. Location of false positives

The argument of subsection II F suggests that false positives are more likely to be found near PS. To validate this proposition, each detected false positive is placed at the center of the corresponding square element and its max-norm distance (27) to the nearest PS is calculated. This distance must be larger than $\Delta x/2$ otherwise it would be a true positive by definition. If that distance is smaller than $3\Delta x/2$, it means that a false positive is detected in a square element adjacent to the one containing a PS. The histogram of these distances for all false positives from 160,000 phase maps are calculated and displayed in Fig. 9. The histograms are normalized by their maximum count to emphasize the decay with the distance.

The results demonstrate that, in this model, false positives are mostly located in the vicinity of PS (Fig. 9). The average distance increases with noise (panel A) and distortion
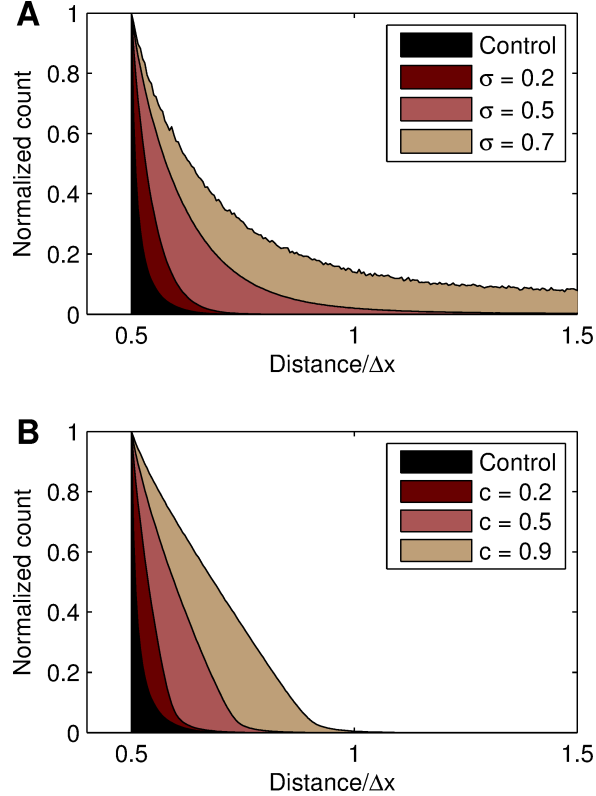
22

FIG. 9. Normalized histograms of the max-norm distance between a false positive and the nearest PS. The distance is expressed in units of interelectrode distance Δx. (A) Effect of noise variance σ. (B) Effect of distortion parameter c.

(panel B), but generally remains within the nearest neighbor square elements. An exception is when noise is sufficiently large ($\sigma > 0.5$) to create false positives in the absence of phase gradient, causing a background density of false positives throughout the mapping area (Fig. 9A, $\sigma = 0.7$).

IV. DISCUSSION

Our statistical model provides a theoretical framework for studying and comparing PS detection methods. Despite its simplifications, this model involves ubiquitous mechanisms of false positives and false negatives caused by PS distribution and steepness of phase gradient that are expected to be present in any model of cardiac reentry. It essentially gives a minimal baseline model on top of which perturbations such as noise or distortion can be added.

The advantage of this approach is the ability to simulate hundreds of millions of independent configurations as required to achieve accurate prediction of false detection rates, particularly when these rates are low and theoretical relations are sought. Indeed, the distribution of false detection number is discrete and the probability of non-zero false detection may be small. The standard error on the mean (Fig. 5) quantifies this requirement. A second advantage is the exact knowledge of PS number and location to unambiguously identify false positives and false negatives. Even in high resolution simulations where phase maps can be derived from the time course of the membrane potential, there are still false detections,[19] making it difficult to define an objective gold standard. A third advantage is its independence from the method to compute the phase map. The results depend solely on the nature of the phase map at a time instant. This may provide guidelines on how to best design phase calculation algorithms. For instance, since distortion increases false detection, it is desirable to define the phase such that the phase distribution is as uniform as possible. The use of Hilbert transform is a step in this direction.[15,17]

The main result of this paper is the set of curves presenting the mean number of false detections (Figs. 6, 7, 8). In this model, the ratio (ξ) between interelectrode distance and mean distance between neighboring PS is shown to be the parameter determining false positive and false negative rates. The square of this parameter corresponds to PS density over the mapping system. Asymptotic power laws for false detection facilitate interpolation or extrapolation. The mapping resolution needed to detect PS with predefined false positive and false negative rates can be read on these figures. As expected, the presence of noise and distortion limits the ability to reduce false detection by increasing mapping resolution.

The constraint on ξ can be linked to tissue wavelength (WL) defined as the spatial separation between successive wave fronts. Rappel et al.[22] argued that Δx should be smaller than $\text{WL}/4$ to detect a single rotor or a focal activation. This was further validated by Roney et al.[16] using simulations in an atrial model. In the context of the leading circle theory,[2] each spiral rotating around a PS occupies a circular region of radius $\text{WL}/2\pi$, which implies that the distance between neighboring PS is of the order of $\lambda_n = \text{WL}/\pi$. After substitution in the condition $\Delta x < \text{WL}/4$, we would estimate $\xi < \pi/4 \approx 0.785$. This constraint for perfect PS detection is less restrictive than ours but relies on the absence of noise and on the assumption that the rotor is unique.

Our phase map generation model can be easily implemented and may be used to test

PS detection algorithms at the proof-of-concept phase. As illustrative example, we assessed the gain obtained by computing the integral over a larger square ($M > 1$). Significant reduction in false negative rate was observed at high resolution and in the presence of noise or distortion (Figs. 7, 8). False positive rate did not decrease with $M > 1$, but the absolute number of false positives did. When isolated false positives are found away from any true PS as in Roney et al.,[16] the benefits of using $M > 1$ might be even more significant. Combining the detection outcome from multiple paths[20] may also be a solution to improve robustness and reduce false positive rate.

Few simulation studies report separately false negatives and false positives. In general, assessment of PS detection algorithm is based on the average number of detected PS or on the ability to track the core of spirals. Roney et al.[31] simulated an average of $n = 9.6$ PS in a tissue with $L = 10$ cm and Δx from 2 to 10 mm, resulting in a ξ value between 0.12 and 0.59. With $\Delta x = 10$ mm, an average of 11.6 PS were detected. If those additional 2 PS were false positives, our curves (Fig. 8) would suggest that the distortion parameter is $c = 0.7$ (assuming no noise), which is plausible since their phase tend to accumulate around $\pm\pi$. However, the same statistical model would overestimate the false negative rate. Our model was not designed to reproduce the PS distribution of a particular set of simulations in which PS location (and therefore the distance between neighboring PS) may be driven by simulation-specific repolarization heterogeneities.

Among the limitations of the statistical model, the generated phase maps (Fig. 2) do not look like spirals around PS. Instead, these maps are designed to minimize the gradients in order to cause the least number of false detection. In particular, they do not include conduction heterogeneities, which can be a source of false positives. An eikonal approach could be used to generate more realistic maps.[26,28,32,33] This would require to introduce another discretization resolution for the eikonal solver and would result in a much higher computational load. Since the main effect would be an increase of the phase gradient far from the PS, this may lead to additional false positives.

The time evolution of phase maps was purposely ignored in the present paper to explore a wider range of independent configurations. In contrast, Kuklik et al.[20] created synthetic phase distributions on a mapping catheter using random variations of a time series of cycle lengths. PS tracking, and notably studying the life span of PS as a post-processing step, enables the reduction of false detection. The assumed uniform distribution of PS often

generates pairs of neighboring PS with opposite signs that might not be considered relevant if they have a short life span. Failure to detect these pairs contributes to false negative rate, but may not be significant in practical applications. Consequently, our idealized statistical model tends to overestimate false negative rate and underestimate false positive rate.

Benchmarking of PS detection algorithms may be designed in three stages: synthetic maps, simulated maps and experimental maps. Despite its limitations, our model of random phase maps provides an easy-to-implement tool for a first stage of benchmarking over a broad range of configurations with multiple PS, as well as a theoretical framework to study the relations between PS distribution and false detections.

ACKNOWLEDGMENTS

REFERENCES

[1] V. Swarup, T. Baykaner, A. Rostamian, J. P. Daubert, J. Hummel, D. E. Krummen, R. Trikha, J. M. Miller, G. F. Tomassoni, and S. M. Narayan, "Stability of rotors and focal sources for human atrial fibrillation: focal impulse and rotor mapping (firm) of af sources and fibrillatory conduction," J Cardiovasc Electrophysiol **25**, 1284–92 (2014).

[2] S. Nattel, F. Xiong, and M. Aguilar, "Demystifying rotors and their place in clinical translation of atrial fibrillation mechanisms," Nat Rev Cardiol (2017).

[3] K. Umapathy, K. Nair, S. Masse, S. Krishnan, J. Rogers, M. P. Nash, and K. Nanthakumar, "Phase mapping of cardiac fibrillation," Circ Arrhythm Electrophysiol **3**, 105–14 (2010).

[4] R. H. Clayton and M. P. Nash, "Analysis of cardiac fibrillation using phase mapping," Card Electrophysiol Clin **7**, 49–58 (2015).

[5] R. Vijayakumar, S. K. Vasireddi, P. S. Cuculich, M. N. Faddis, and Y. Rudy, "Methodology considerations in phase mapping of human cardiac arrhythmias," Circ Arrhythm

Electrophysiol **9**, e004409 (2016).

[6] A. T. Winfree, *The Geometry of Biological Time*, Interdisciplinary Applied Mathematics (Springer New York, 2001).

[7] A. N. Iyer and R. A. Gray, "An experimentalist's approach to accurate localization of phase singularities during reentry," Ann Biomed Eng **29**, 47–59 (2001).

[8] M.-A. Bray and J. P. Wikswo, "Use of topological charge to determine filament location and dynamics in a numerical model of scroll wave activity," IEEE Trans Biomed Eng **49**, 1086–93 (2002).

[9] S. M. Narayan, T. Baykaner, P. Clopton, A. Schricker, G. G. Lalani, D. E. Krummen, K. Shivkumar, and J. M. Miller, "Ablation of rotor and focal sources reduces late recurrence of atrial fibrillation compared with trigger ablation alone: extended follow-up of the confirm trial (conventional ablation for atrial fibrillation with or without focal impulse and rotor modulation)," J Am Coll Cardiol **63**, 1761–8 (2014).

[10] J. M. Miller, V. Kalra, M. K. Das, R. Jain, J. B. Garlie, J. A. Brewster, and G. Dandamudi, "Clinical benefit of ablating localized sources for human atrial fibrillation: The indiana university firm registry," J Am Coll Cardiol **69**, 1247–1256 (2017).

[11] R. A. Gray, A. M. Pertsov, and J. Jalife, "Spatial and temporal organization during cardiac fibrillation," Nature **392**, 75–8 (1998).

[12] M. A. Bray, S. F. Lin, R. R. Aliev, B. J. Roth, and J. P. Wikswo, "Experimental and theoretical analysis of phase singularity dynamics in cardiac tissue," J Cardiovasc Electrophysiol **12**, 716–22 (2001).

[13] S. Puwal, B. J. Roth, and S. Kruk, "Automating phase singularity localization in mathematical models of cardiac tissue dynamics," Math Med Biol **22**, 335–46 (2005).

[14] M.-A. Bray and J. P. Wikswo, "Considerations in phase plane analysis for nonstationary reentrant cardiac behavior," Phys Rev E Stat Nonlin Soft Matter Phys **65**, 051902 (2002).

[15] P. Kuklik, S. Zeemering, B. Maesen, J. Maessen, H. J. Crijns, S. Verheule, A. N. Ganesan, and U. Schotten, "Reconstruction of instantaneous phase of unipolar atrial contact electrogram using a concept of sinusoidal recomposition and hilbert transform," IEEE Trans Biomed Eng **62**, 296–302 (2015).

[16] C. H. Roney, C. D. Cantwell, N. A. Qureshi, R. A. Chowdhury, E. Dupont, P. B. Lim, E. J. Vigmond, J. H. Tweedy, F. S. Ng, and N. S. Peters, "Rotor tracking using phase of electrograms recorded during atrial fibrillation," Ann Biomed Eng **45**, 910–923 (2017).

[17]L. A. Unger, M. Rottmann, G. Seemann, and O. Dössel, "Detecting phase singularities and rotor center trajectories based on the hilbert transform of intraatrial electrograms in an atrial voxel model," Current Directions in Biomedical Engineering **1**, 38–41 (2015).

[18]L. J. Rantner, L. Wieser, M. C. Stuhlinger, F. Hintringer, B. Tilg, and G. Fischer, "Detection of phase singularities in triangular meshes," Methods Inf Med **46**, 646–54 (2007).

[19]R. Zou, J. Kneller, L. J. Leon, and S. Nattel, "Development of a computer algorithm for the detection of phase singularities and initial application to analyze simulations of atrial fibrillation," Chaos **12**, 764–778 (2002).

[20]P. Kuklik, S. Zeemering, A. van Hunnik, B. Maesen, L. Pison, D. Lau, J. Maessen, P. Podziemski, C. Meyer, B. Schaffer, H. Crijns, S. Willems, and U. Schotten, "Identification of rotors during human atrial fibrillation using contact mapping and phase singularity detection: Technical considerations," IEEE Trans Biomed Eng **64**, 310–318 (2016).

[21]C. H. Roney, C. D. Cantwell, J. D. Bayer, N. A. Qureshi, P. B. Lim, J. H. Tweedy, P. Kanagaratnam, N. S. Peters, E. J. Vigmond, and F. S. Ng, "Spatial resolution requirements for accurate identification of drivers of atrial fibrillation," Circ Arrhythm Electrophysiol **10**, e004899 (2017).

[22]W.-J. Rappel and S. M. Narayan, "Theoretical considerations for mapping activation in human cardiac fibrillation," Chaos **23**, 023113 (2013).

[23]N. Bursac, F. Aguel, and L. Tung, "Multiarm spirals in a two-dimensional cardiac substrate," Proc Natl Acad Sci U S A **101**, 15530–4 (2004).

[24]R. Zou, J. Kneller, L. J. Leon, and S. Nattel, "Substrate size as a determinant of fibrillatory activity maintenance in a mathematical model of canine atrium," Am J Physiol Heart Circ Physiol **289**, H1002–12 (2005).

[25]K. S. McDowell, S. Zahid, F. Vadakkumpadan, J. Blauer, R. S. MacLeod, and N. A. Trayanova, "Virtual electrophysiological study of atrial fibrillation in fibrotic remodeling," PLoS One **10**, e0117110 (2015).

[26]A. Herlin and V. Jacquemet, "Eikonal-based initiation of fibrillatory activity in thin-walled cardiac propagation models," Chaos **21**, 043136 (2011).

[27]G. Kochenberger, J.-K. Hao, F. Glover, M. Lewis, Z. Lu, H. Wang, and Y. Wang, "The unconstrained binary quadratic programming problem: a survey," J. Combinatorial Optimization **28**, 58–81 (2014).

[28] A. Herlin and V. Jacquemet, "Reconstruction of phase maps from the configuration of phase singularities in two-dimensional manifolds," Phys Rev E **85**, 051916 (2012).

[29] K. Mardia and P. Jupp, *Directional Statistics*, Wiley Series in Probability and Statistics (Wiley, 2009).

[30] P. Bhattacharyya and B. K. Chakrabarti, "The mean distance to the nth neighbour in a uniform distribution of random points: an application of probability theory," Eur. J. Phys. **29**, 639 (2008).

[31] C. H. Roney, C. D. Cantwell, J. H. Siggers, F. S. Ng, and N. S. Peters, "A novel method for rotor tracking using bipolar electrogram phase," in *Computing in Cardiology* (IEEE, 2014) pp. 233–236.

[32] V. Jacquemet, "An eikonal approach for the initiation of reentrant cardiac propagation in reaction-diffusion models," IEEE Trans Biomed Eng **57**, 2090–2098 (2010).

[33] V. Jacquemet, "An eikonal-diffusion solver and its application to the interpolation and the simulation of reentrant cardiac activations," Comput Methods Programs Biomed **108**, 548–58 (2012).